


Collective effects and pattern formation for directional locking of disks moving through obstacle arrays

C. Reichhardt and C. J. O. Reichhardt ^{*}*Theoretical Division and Center for Nonlinear Studies, Los Alamos National Laboratory, Los Alamos, New Mexico 87545, USA*

(Received 10 June 2020; accepted 31 July 2020; published 18 August 2020)

We examine directional locking effects in an assembly of disks driven through a square array of obstacles as the angle of drive rotates from 0° to 90° . For increasing disk densities, the system exhibits a series of different dynamic patterns along certain locking directions, including one-dimensional or multiple-row chain phases and density-modulated phases. For nonlocking driving directions, the disks form disordered patterns or clusters. When the obstacles are small or far apart, a large number of locking phases appear; however, as the number of disks increases, the number of possible locking phases drops due to the increasing frequency of collisions between the disks and obstacles. For dense arrays or large obstacles, we find an increased clogging effect in which immobile and moving disks coexist.

DOI: [10.1103/PhysRevE.102.022608](https://doi.org/10.1103/PhysRevE.102.022608)

I. INTRODUCTION

In directional locking, the motion of a particle driven over a periodic substrate such as a square lattice tends to remain locked at certain symmetry directions of the lattice as the driving direction is varied [1–6]. For a square lattice, the strongest directional locking appears when the angle θ between the driving direction and the lattice symmetry direction is near $\theta = 0^\circ$, 45° , or 90° ; however, locking can occur for any rational ratio p/q with integer p and q , where the particle moves exactly p lattice constants in the x direction and q lattice constants in the y direction during some time interval. In this case, the directional locking is centered at an angle $\theta_L = \arctan(p/q)$, so that $p/q = 0$ corresponds to $\theta_L = 0^\circ$ and $p/q = 1$ gives $\theta_L = 45^\circ$. Locking occurs whenever $\theta = \theta_L \pm \Delta\theta$, where the width of an individual locking step is defined to be $2\Delta\theta$, and the step width is largest for small values of p and q . This behavior is similar to the Bragg angle scattering conditions found for a lattice. A devil's staircase hierarchy of locking steps can appear in the angle of the particle motion as a function of the driving angle θ .

Directional locking effects have similarities to the phase locking phenomena observed in systems with two competing frequencies. For example, if a particle moving over a one-dimensional (1D) periodic substrate under a dc drive is subjected to an additional ac drive in the direction of motion, locking effects arise due to the interaction between the frequency ω_1 generated by the dc motion of the particle over the substrate and the ac driving frequency ω_2 . When ω_2 is fixed, the particle velocity locks to a constant value over a range of dc drive amplitudes in order to maintain resonance [7–9]. Varying the dc drive changes ω_1 , so a series of steps known as Shapiro steps appear in the velocity-force curve at rational values of ω_1/ω_2 [7–9]. Directional locking was first

studied for vortices in type II superconductors driven in a changing direction over a periodic pinning lattice and occurs when the direction of vortex motion becomes locked to one of the substrate symmetry directions [1]. The substrate lattice structure determines the set of possible directional locking angles, while the widths of the locking steps can be changed by varying the strength of the pinning. The lattice over which the superconducting vortices move is composed of attractive pinning sites which the vortices must traverse during a locking step. Due to the relatively long range of the vortex-vortex interactions, the vortices form a moving lattice or ordered structure on the locking steps, whereas when the motion is not locked, the vortex structure is more disordered or liquidlike [1,10].

Following the vortex work, similar directional locking effects were proposed to occur for classical electrons moving over a square antidot lattice [2]. Here, the direction of drive is controlled by the applied magnetic field, since a larger magnetic field produces a larger Hall angle. In the presence of a periodic array of scattering sites, the Hall angle becomes quantized with steps at rational values of p/q , where the electron translates by an integer number p and q of substrate lattice constants in the x and y directions, respectively, during a period of time.

The first experimental observations of directional lockings were obtained using colloidal particles moving over a square optical trap array. When the driving direction is fixed but the substrate lattice is rotated, the colloidal motion locks to different symmetry angles [3]. The width $2\Delta\theta$ of the locking steps depends on the interaction of the particle with the pinning site or obstacle, implying that if two species of particles are present, and each interacts differently with the substrate, the driving conditions can be tuned such that one species locks to the substrate and the other does not. As a result, each species moves at a different angle, making it possible to achieve a spatial separation or fractionation of the species. This sorting effect based on directional locking

^{*}cjrx@lanl.gov

was first demonstrated experimentally by MacDonald *et al.* for colloids of different sizes and different refractive indexes [5]. Directional locking and sorting effects have been studied extensively for colloidal systems under different conditions and geometries, taking into account a variety of dynamical effects and particle-substrate interactions [5,11–26]. Directional locking for particles on periodic substrates has also been studied in the context of skyrmions in chiral magnets. Skyrmions are particlelike magnetic textures or bubbles which exhibit a Hall angle that changes with increasing driving force in the presence of a substrate [27–29]. There are also a number of systems in which particles moving over periodic substrates under different driving conditions preferentially move in certain directions due to the underlying symmetry of the substrate. This effect has been studied for magnetic colloids undergoing oscillatory motion [30,31] and for active matter on periodic obstacle arrays [32,33].

In many studies of directional locking, the dynamics is effectively in the single-particle limit; however, when collective effects become important, such as when a large number of interacting particles are present, changes in the locking behavior can occur that include modifications of locking step widths or the formation of different types of patterns in locking and nonlocking regimes. Collective effects of this type were studied for superconducting vortices on a periodic pinning array, and they can also appear for vortices or colloids moving over quasiperiodic arrays, where for certain driving directions the system forms moving smectic, square, triangular lattice, or disordered phases [34]. Several of these phases have been observed in experiments on colloids moving over quasiperiodic pinning arrays [35]. In the superconducting vortex system, the directional locking step widths oscillate as a function of the magnetic field, with wider steps or stronger locking occurring when the number of vortices is an integer multiple of the number of pinning sites [36–39].

More recently, the impact of collective effects on locking phases was studied for colloidal clusters where each individual cluster can have different orientations that lock to the orientation of the underlying substrate lattice [40,41]. Similar effects were observed for the motion of Au islands on two-dimensional (2D) atomic substrates [42]. Recent studies focused on collective locking effects for colloids moving over triangular substrate arrays, where certain driving directions have two equivalent locking directions. If the particles do not interact with each other, no net directional locking occurs, but when particle-particle interactions are added, a global locking effect appears due to a dynamical symmetry breaking. The direction of this symmetry breaking can be controlled using a small biasing field [43]. Similar spontaneous dynamic symmetry breaking leading to directional locking has also been found in simulations of colloids [44] and vortices [45] on periodic substrate arrays.

Up until now, collective locking on pinning arrays has been studied for particles with relatively long-range interactions, such as superconducting vortices or charged colloids. Far less is known about the impact of collective effects on locking when the particles have short-range interactions and are moving over arrays of repulsive obstacles or posts. A limited study addressed the dense particle limit of bidisperse disks moving through a square obstacle array and showed that a clogged

state can appear in which the disk density becomes strongly inhomogeneous and the disks pile up behind each other [46]. In this case, the clogging susceptibility depends on the drive angle, with clogging occurring much more readily at certain driving angles.

In this work we study directional locking for a monodisperse assembly of disks moving through a square array of obstacles where we vary the density of the moving disks as well as the radius and lattice constant of the obstacles. For low disk densities and small obstacle sizes, strong directional locking occurs and the system is nearly always in a locked state with $\theta_L = \arctan(p/q)$. As the disk density increases, fewer locking steps appear and the disks form 1D chains at certain driving directions. For higher disk densities, the chains thicken and we find that two to three rows of disks can move between adjacent obstacles. When an integer number of rows of moving disks is unable to form, the locking effects are lost. This is similar to the frustration effect found for the ordering of rows of disks on quasi-1D substrates. On other locking steps, the system forms a density-modulated state where the overall configuration is disordered but the trajectories of individual disks are ordered. In the nonlocking regimes, the disk configurations are more disordered and mixing of the disks occurs. The velocity of the disks in a locking region is not constant but changes nonmonotonically with driving angle θ , exhibiting peaks and valleys. In contrast, the direction of disk motion is constant on a locking step. There are pronounced cusps and dips in the disk velocity at the transitions into and out of the locking phases. At high disk densities, we find that the $p/q = 1.0$ locking step is lost due to a dynamical frustration effect, but some other locking phases remain present. When the obstacle size is increased in a system with a fixed disk density, the width of the locking phases varies nonmonotonically and a clogging effect emerges in which a portion of the disks becomes blocked behind the obstacles. The amount of clogging that occurs depends on the direction of driving, and the disks are able to slide more easily when the drive is aligned with 0° , 90° , or 45° . For the largest obstacles or for high disk densities, we find a complete clogging where all disk flow ceases. When the disk density and obstacle size are held constant but the obstacle lattice constant is increased, the number of locking steps increases but the width of the locking phases is reduced. Our results should be relevant to the flow of uncharged colloids, bubbles or emulsions over obstacle arrays and suggest new ways to generate different dynamical patterns.

II. SIMULATION

We consider a 2D system of size $L \times L$ with periodic boundary conditions in the x and y directions where $L = 36$. The sample contains a square lattice of N_{obs} obstacles modeled as harmonically repulsive posts with radius R_{obs} and lattice constant a , as well as N_d harmonically repulsive disks of radius R_d . The overall system density ϕ is defined to be the total area covered by both obstacles and disks, $\phi = (N_{\text{obs}}\pi R_{\text{obs}}^2 + N_d\pi R_d^2)/L^2$. The dynamics of disk i is obtained by integrating the following overdamped equation of motion:

$$\alpha_d \mathbf{v}_i = \mathbf{F}_i^{dd} + \mathbf{F}_i^{\text{obs}} + \mathbf{F}^D. \quad (1)$$

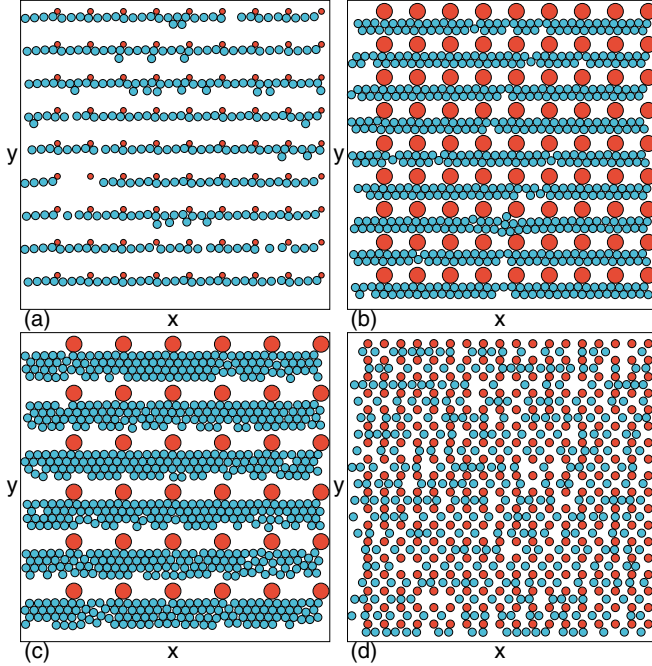


FIG. 1. The obstacle locations (red circles) and the mobile disks (blue circles) for a system with disk radius $R_d = 0.5$ and driving force $F^D = 0.5$ applied at an angle $\theta = 3^\circ$ from the positive x axis. The disk motion is locked to $\theta_L = 0^\circ$. (a) Obstacle lattice constant $a = 4.0$ and radius $R_{\text{obs}} = 0.35$ at a total disk density of $\phi = 0.217$. (b) For $a = 4.0$, $R_{\text{obs}} = 1.0$, and a larger number of mobile disks giving $\phi = 0.57$, there are two mobile rows of disks between each row of obstacles. (c) $a = 6.0$, $R_{\text{obs}} = 1.0$, and $\phi = 0.55$, where a density-modulated state appears. (d) $a = 2.0$, $R_{\text{obs}} = 0.5$, and $\phi = 0.242$.

Here \mathbf{r}_i is the disk position, $\mathbf{v}_i = d\mathbf{r}_i/dt$ is the disk velocity, and α_d is the damping constant, which we set to $\alpha_d = 1.0$. The disk-disk interaction force is \mathbf{F}_i^{dd} and the disk-obstacle interaction force is $\mathbf{F}_i^{\text{obs}}$, while the driving force is $\mathbf{F}^D = F^D \cos(\theta)\hat{\mathbf{x}} + F^D \sin(\theta)\hat{\mathbf{y}}$. We gradually increase θ from 0 so that \mathbf{F}^D is initially aligned with the x direction and rotates into the y direction. We measure the average velocity in the x and y directions, $\langle V_x \rangle = \sum_{i=1}^{N_d} \mathbf{v}_i \cdot \hat{\mathbf{x}}$ and $\langle V_y \rangle = \sum_{i=1}^{N_d} \mathbf{v}_i \cdot \hat{\mathbf{y}}$, as well as the net velocity, $\langle V \rangle = \sqrt{\langle V_x \rangle^2 + \langle V_y \rangle^2}$. The drive is fixed to $F^D = 0.5$ and we increment θ by an amount $\Delta\theta = 0.057^\circ$ every 10^4 simulation time steps. We have also used slower increment rates for the smaller obstacle radii in order to resolve the higher-order directional locking effects.

III. VARIED DISK DENSITY

In Fig. 1 we illustrate the positions of the disks and obstacles for a disk radius of $R_d = 0.5$ when the driving angle has reached $\theta = 3^\circ$. In the absence of a substrate the disks would move along the θ direction, but in the presence of obstacles the motion locks to $\theta_L = 0^\circ$, corresponding to $p/q = 0$, due to the symmetry of the substrate lattice. In Fig. 1(a), the obstacle lattice constant is $a = 4.0$, the obstacle radius is $R_{\text{obs}} = 0.35$, and the sample contains $N_{\text{obs}} = 81$ obstacles and $N_d = 319$ disks, for a total density of $\phi = 0.217$. Here the disks form nearly 1D chains of single rows which brush up against the

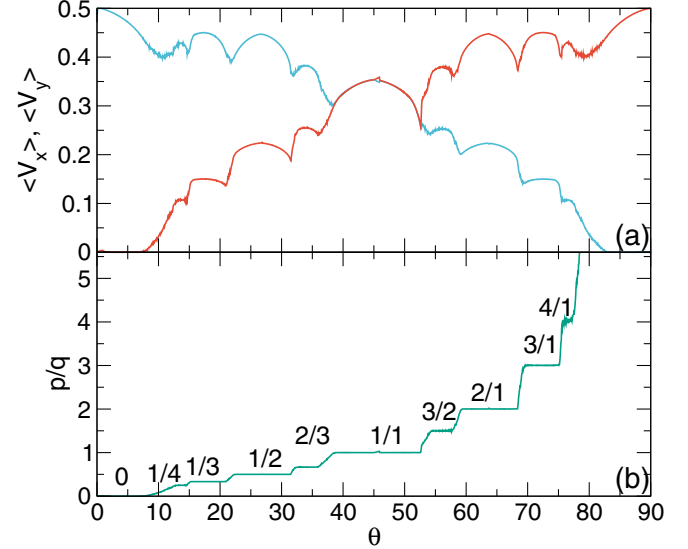


FIG. 2. (a) Velocities $\langle V_x \rangle$ in the x direction (blue curve) and $\langle V_y \rangle$ in the y direction (red curve) vs drive angle θ for the system in Fig. 1(a) with $a = 4.0$, $R_{\text{obs}} = 0.35$, and $\phi = 0.217$. (b) p/q or $\langle V_y \rangle / \langle V_x \rangle$ vs θ showing a series of directional locking steps. The steps at 0, 1/4, 1/3, 1/2, 2/3, 1/1, 3/2, 2/1, 3/1, and 4/1 are highlighted.

obstacles due to the nonzero driving angle. In Fig. 1(b), we show the same system for a larger obstacle radius $R_{\text{obs}} = 1.0$ and larger number of disks $N_d = 619$, giving a total density of $\phi = 0.57$. The disks now form stripes composed of two rows of disks. For a system with $a = 6.0$, $R_{\text{obs}} = 1.0$, and $\phi = 0.55$, Fig. 1(c) indicates that the disks form a density-modulated state in which stripes appear that are almost four disks wide. In Fig. 1(d), the disks in a sample with $a = 2.0$, $R_{\text{obs}} = 0.5$, and $\phi = 0.242$ are more uniformly distributed.

In Fig. 2(a) we plot $\langle V_x \rangle$ and $\langle V_y \rangle$ versus the angle θ of the system in Fig. 1(a) at a drive of $F^D = 0.5$, while in Fig. 2(b) we show the corresponding value of p/q or $\langle V_y \rangle / \langle V_x \rangle$ versus θ . The velocity steps in Fig. 2(a) are not flat but take the form of rounded humps bracketed by cusps at the jumps in and out of the locking phases. In contrast, we do find flat steps in the value of p/q , indicating that although the velocity of the disks is changing, the direction of disk motion is fixed. On the 1/1 step, Fig. 2(b) indicates that the direction of motion is locked over a fixed interval centered at $\theta = 45^\circ$, while prominent steps also appear at $p/q = 0, 1/4, 1/3, 1/2, 2/3, 1, 3/2, 2, 3,$ and 4 . The upper edge of the $p/q = 0$ locking step falls at $\theta = 7^\circ$.

In Fig. 3(a) we show a snapshot of the disks from the system in Fig. 2 at $\theta = 11.5^\circ$ where the motion is not locked and the disk structure is disordered. Figure 3(b) illustrates the $p/q = 1/3$ locking step in the same system at a drive angle of $\theta = 18.4^\circ$, where the disks are more ordered and have a weak density modulation perpendicular to the driving direction. In Fig. 3(c) we plot the disk trajectories during a fixed time for the sample in Fig. 3(a). The trajectories are disordered, with a mixing character, and over long times a given disk diffuses gradually through the sample, indicating that this is a liquid state. Figure 3(d) shows the trajectories for the $p/q = 1/3$ step

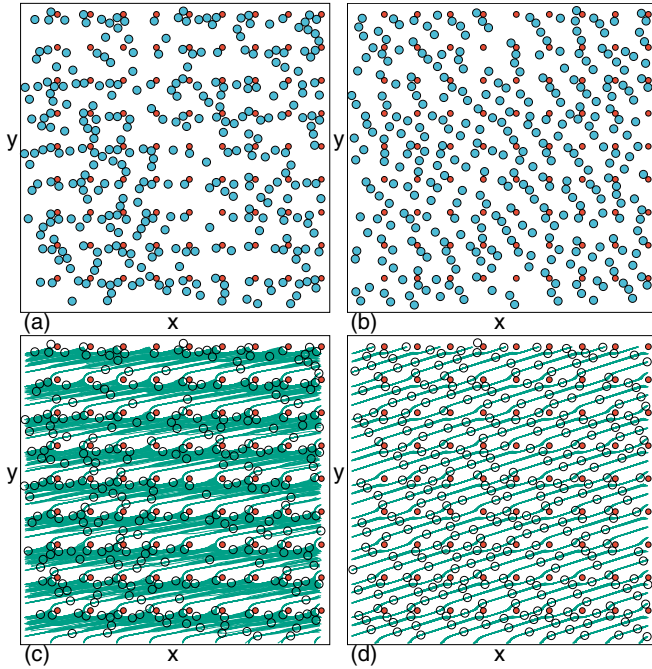


FIG. 3. (a) Obstacle (red circles) and disk (blue circles) locations for the system in Fig. 2 with $a = 4.0$, $R_{\text{obs}} = 0.35$, $\phi = 0.217$, and $R_d = 0.5$. (a) A nonlocking regime at a drive angle of $\theta = 11.5^\circ$, where the disk configuration is disordered. (b) The $p/q = 1/3$ step at a drive angle of $\theta = 18.4^\circ$, where the disks are more ordered. (c) Disordered disk trajectories (green lines) for the system in (a). (d) One-dimensional ordered disk trajectories for the system in (b). In (c) and (d), the mobile disks are drawn as open circles for clarity.

from Fig. 3(b), where the trajectories are strongly ordered and form 1D patterns oriented along $\theta_L = \arctan(1/3) = 18.435^\circ$. Here, each disk maintains the same neighbors as it moves, and there is no long-time diffusion.

In general, the disk motion is more ordered along the locking steps and more disordered or liquid in the nonlocking regimes; however, within the locking regions, different structures can arise. In Fig. 4(a) we plot the disk positions for the system in Fig. 2 at the $p/q = 1/2$ step where a partially square lattice appears. On the $p/q = 2/3$ step in Fig. 4(b), the configuration is disordered but shows some partial clustering or density modulation. Figure 4(c) illustrates the disk positions in a nonstep region just below the $p/q = 1/1$ step, where the system is disordered but the density is uniform. On the $p/q = 1/1$ locking step in Fig. 4(d), we find ordered 1D chains aligned at 45° such that the disks do not collide with the obstacles. At $p/q = 3/1$ in Fig. 4(e), a strongly density modulated state appears, while in Fig. 4(f) on the 90° locking step, a series of nearly 1D chains form that are aligned with the y direction. The 1D lanes on the 90° step are more ordered than the lanes found on the 0° step in Fig. 1(a). This is the result of the partial dynamic annealing produced when the disks pass through multiple fluctuating nonlocked regions before reaching the 90° locking step. The fluctuating states allow the disks to reach more ordered configurations, whereas on the 0° locking step, the disks remain trapped in their initial configuration. The difference in ordering between the 0° and

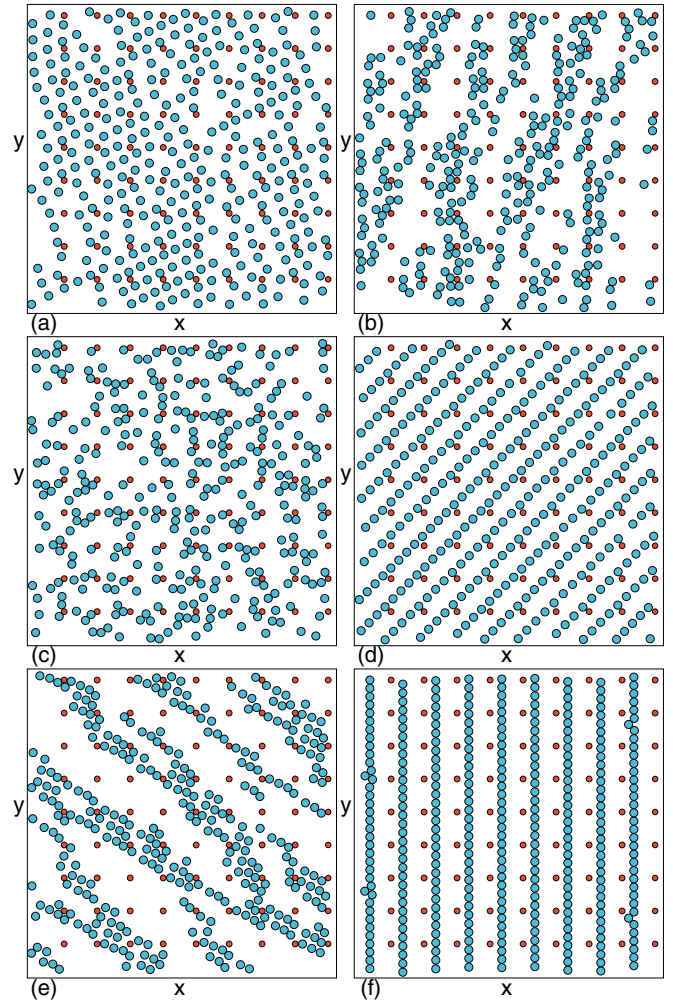


FIG. 4. Obstacle (red circles) and disk (blue circles) locations for the system in Fig. 2 with $a = 4.0$, $R_{\text{obs}} = 0.35$, $\phi = 0.217$, and $R_d = 0.5$. (a) A square lattice configuration at $p/q = 1/2$. (b) Cluster formation at $p/q = 2/3$. (c) A disordered configuration just below the $p/q = 1/1$ locking step. (d) Ordered 1D chains at $p/q = 1/1$. (e) A density-modulated phase at $p/q = 3/1$. (f) Nearly 1D channels at the 90° locking step.

the 90° steps would be less pronounced if the temperature were finite.

In Fig. 5 we plot the disk positions and trajectories for the system in Fig. 4. At $p/q = 1/2$ in Fig. 5(a), the disks follow 1D paths and move a distance $2a$ in the x direction for each translation by a in the y direction. No collisions occur between the moving disks and the obstacles. Figure 5(b) shows that the trajectories are disordered for the system in Fig. 4(c) just below the $p/q = 1/1$ locking step. In Fig. 5(c), the trajectories on the $p/q = 1/1$ step exhibit ordered 1D motion. At $p/q = 3/1$ in Fig. 5(d), the disks form a disordered density-modulated phase in which the trajectories are ordered. In general, for the locking phases the disks move elastically and maintain the same neighbors, while in the nonlocking phases, the disks diffuse with respect to each other, forming a liquid state.

In Fig. 6 we plot the net velocity $\langle V \rangle = \sqrt{\langle V_x \rangle^2 + \langle V_y \rangle^2}$ versus θ for the system in Fig. 2 at densities of $\phi = 0.096$,

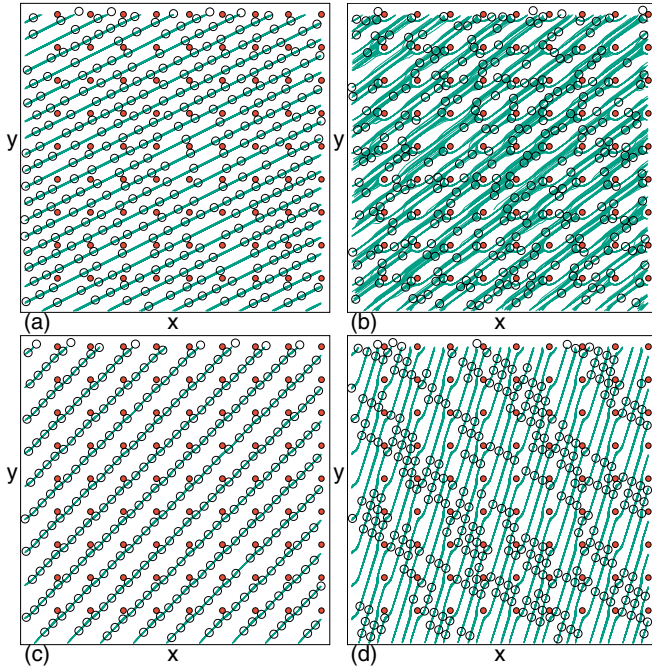


FIG. 5. Obstacle (red circles) and disk (open circles) locations along with disk trajectories (green symbols) for the system in Fig. 2 with $a = 4.0$, $R_{\text{obs}} = 0.35$, $\phi = 0.217$, and $R_d = 0.5$. (a) One-dimensional trajectories at $p/q = 1/2$. (b) Disordered trajectories in the nonstep region just below the $p/q = 1/1$ locking step. (c) At $p/q = 1/1$, the disks move in 1D chains along $\theta_L = 45^\circ$. (d) At $p/q = 3/1$, the system forms a density-modulated phase with ordered trajectories.

0.217, 0.3857, 0.46, and 0.558. The net velocity passes through a local maximum at the center of each locking regime, corresponding to the points at which the interactions between the disks and the obstacles are minimized. For the lowest density of $\phi = 0.096$, we find a range of values $0.35 < \langle V \rangle <$

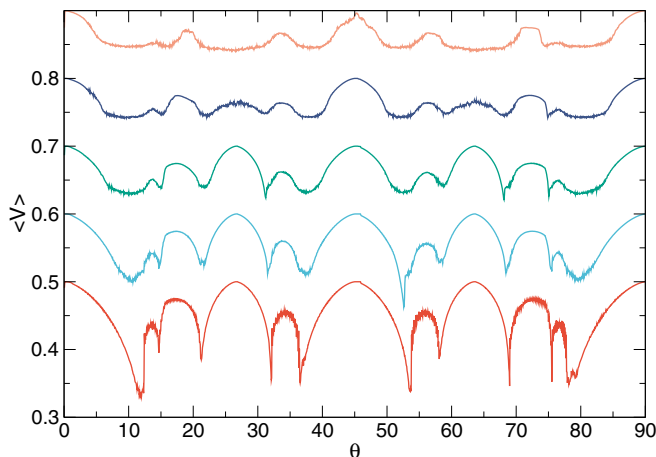


FIG. 6. Net velocity $\langle V \rangle$ vs θ for the system in Fig. 2 with $a = 4.0$, $R_{\text{obs}} = 0.35$, and $R_d = 0.5$ at densities $\phi = 0.096$ (red curve), 0.217 (light-blue curve), 0.3857 (green curve), 0.46 (dark-blue curve), and 0.558 (orange curve), from bottom to top. The curves have been shifted vertically by intervals of 0.1 for clarity.

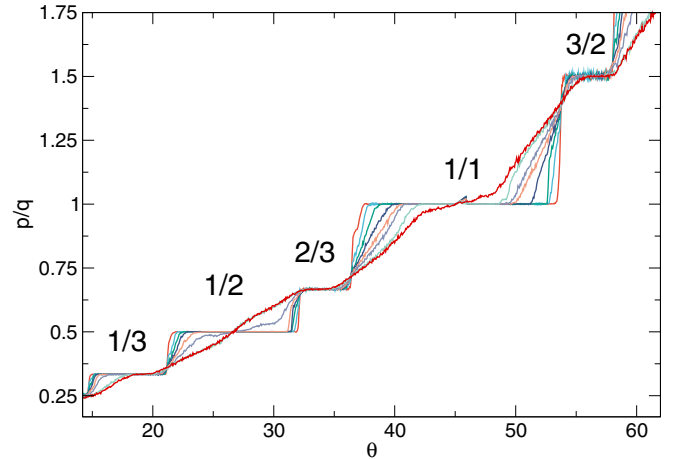


FIG. 7. p/q vs θ for the system in Fig. 6 with $a = 4.0$, $R_{\text{obs}} = 0.35$, and $R_d = 0.5$ at $\phi = 0.096$ (dark-orange curve), 0.1567 (light-blue curve), 0.217 (dark-green curve), 0.278 (dark-blue curve), 0.3857 (light-orange curve), 0.46 (light-purple curve), 0.52 (light-green curve), and 0.558 (red curve). The steps gradually disappear as the disk density increases.

0.5. The maximum velocity cannot exceed the driving force value, $F^D = 0.5$. We obtain $\langle V \rangle = F^D$ whenever the moving disks cease interacting with the obstacles, which occurs for $p/q = 0, 1/2, 1/1$ and in the 90° locking phase. Here the disks move in 1D chains and do not come into contact with the obstacles, as illustrated in Fig. 5(a) for $p/q = 1/2$ and in Fig. 4(d) for $p/q = 1/1$. Some of the directionally locked regimes have a reduced maximum velocity due to disk-obstacle collisions, as shown in Fig. 5(d) for $p/q = 3/1$ and in Fig. 3(d) for $p/q = 1/3$. The lowest velocity values appear in the nonlocking regimes. As the density of mobile disks increases, the number of locked phases diminishes and the maxima and minima in $\langle V \rangle$ become less distinct. For example, at the highest density of $\phi = 0.58$, we find only small peaks in $\langle V \rangle$ at $p/q = 1/3, 2/3, 1/1, 3/2$, and $3/1$, while the peaks at $1/4, 1/2, 2/1$, and $4/1$ have disappeared.

The evolution of the locking regimes is illustrated in the plot of p/q versus θ at different values of ϕ in Fig. 7. The $p/q = 1/3, 2/3$, and $3/2$ steps decrease in width as ϕ increases but remain present even for the highest disk densities, whereas the $p/q = 1/2$ locking step disappears when $\phi > 0.5$. At $\phi = 0.46$, the $1/2$ step is partially locked and p/q does not remain constant on the step but shows a linear increase. For the $p/q = 1/1$ step, complete locking is lost when $\phi > 0.53$ and there is only partial locking at $\phi = 0.558$.

Based on curves such as those shown in Fig. 7, we construct a phase diagram highlighting the different locking phases. In Fig. 8 we plot the locations of the locked phases as a function of θ versus ϕ . The most prominent locking steps appear at $p/q = 1/1, 0^\circ$, and 90° . The $p/q = 1/2$ and $2/1$ steps disappear when $\phi > 0.4$ and the disks become dense enough that 1D ordered chains can no longer form. In general, the widths of all of the steps decrease with increasing ϕ .

In Fig. 9(a) we illustrate the disk configurations for the system in Fig. 8 at $\phi = 0.52$ and $p/q = 1/3$, where a directional locking step occurs and the disks are partially ordered. In the

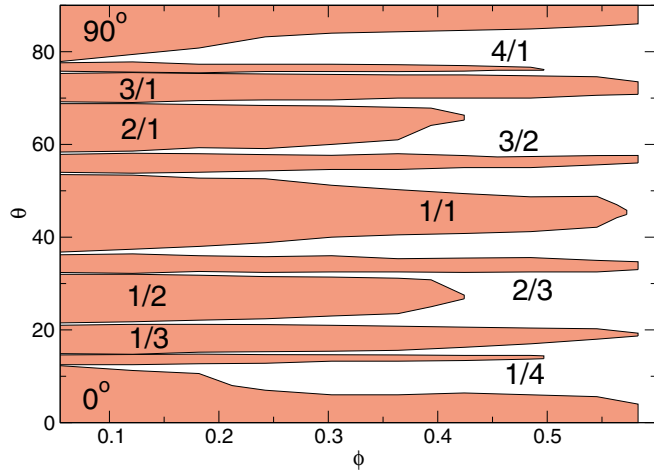


FIG. 8. Locked regions (shaded areas) as a function of θ vs disk density ϕ for the system in Fig. 7 with $a = 4.0$, $R_{\text{obs}} = 0.35$, and $R_d = 0.5$. The $p/q = 0, 1/4, 1/3, 1/2, 2/3, 1/1, 3/2, 2/1, 3/1, 4/1$, and 90° steps are labeled. The $p/q = 1/2$ and $2/1$ steps are the first to disappear as ϕ increases.

same system at $p/q = 1/2$, Fig. 9(b) shows that the disks are much more disordered and there is no directional locking. In general, as the disk density increases, it is more difficult for the disks to move around the obstacles in an ordered fashion in order to form a locked state.

The width of the locking steps as a function of ϕ is affected by the value of the obstacle radius R_{obs} . In Fig. 10(a) we plot $\langle V_x \rangle$ and $\langle V_y \rangle$ versus θ for the system from Fig. 1 with $R_{\text{obs}} = 1.0$, $R_d = 0.5$, and $\phi = 0.39$, while in Fig. 10(b) we show the corresponding p/q versus θ . Here, locking steps appear only for $p/q = 0, 1/2, 1/1, 2/1$, and 90° . Figures 10(c) and 10(d) show $\langle V_x \rangle$, $\langle V_y \rangle$, and p/q versus θ for the same system at the higher mobile disk density of $\phi = 0.57$. Locking occurs only at angles of 0° and 90° , while the other locking steps are lost.

In Fig. 11(a) we show the disk configurations and trajectories for the system in Fig. 10(a) on the $p/q = 1/2$ locking step where the system forms a partially clustered state with ordered trajectories. Figure 11(b) illustrates the disordered disk trajectories that appear in the same system at $\phi = 0.51$

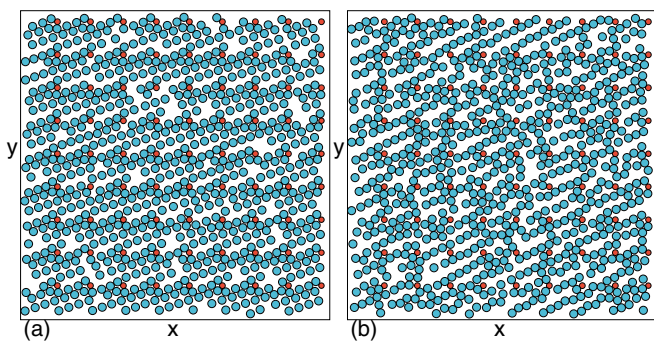


FIG. 9. (a) Obstacle (red circles) and disk (blue circles) locations for the system in Fig. 8 with $a = 4.0$, $R_{\text{obs}} = 0.35$, and $R_d = 0.5$ at $\phi = 0.52$. (a) At $p/q = 1/3$, there is a locking step and the disk positions are partially disordered. (b) At $p/q = 1/2$, there is no directional locking and the disk configuration is disordered.

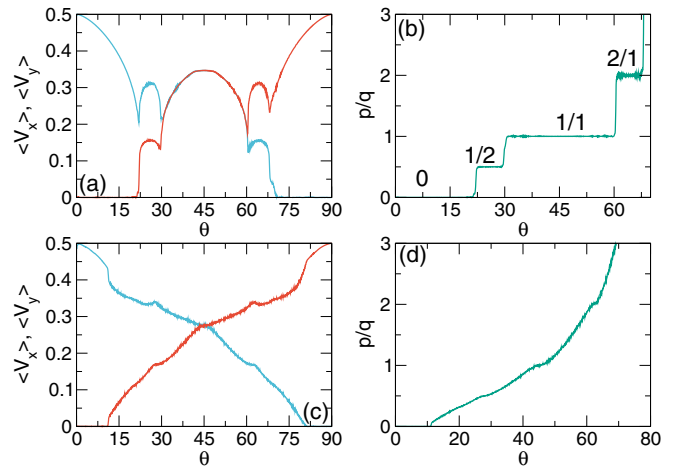


FIG. 10. (a) $\langle V_x \rangle$ (blue curve) and $\langle V_y \rangle$ (red curve) vs θ for the system in Fig. 1 with $a = 4.0$, $R_{\text{obs}} = 1.0$, $R_d = 0.5$, and $\phi = 0.39$. (b) The corresponding p/q vs θ showing locking steps at $p/q = 0, 1/2, 1/1, 2/1$, and 90° . (c) $\langle V_x \rangle$ (blue curve) and $\langle V_y \rangle$ (red curve) vs θ for the system in Fig. 1(b) with $\phi = 0.57$, where locking steps appear only at 0° and 90° . (d) The corresponding p/q vs θ .

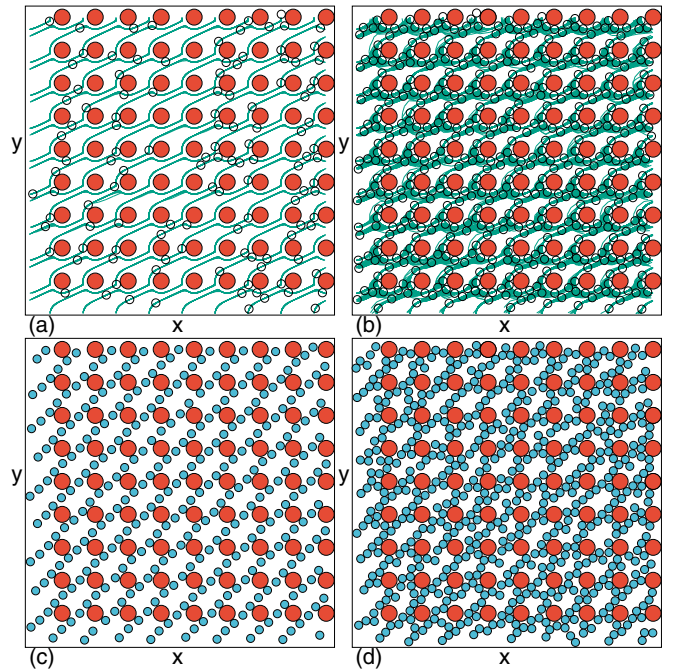


FIG. 11. (a) Obstacle (red circles) and disk (blue and open circles) locations along with disk trajectories (green symbols) for the system in Fig. 10(a) with $a = 4.0$, $R_{\text{obs}} = 1.0$, $R_d = 0.5$, and $\phi = 0.39$ in the $p/q = 1/2$ locking phase where the disk configurations are heterogeneous but the trajectories are ordered. (b) The same system at a higher mobile disk density of $\phi = 0.51$ in the nonlocking regime just above the $p/q = 1/2$ locking step, where the trajectories are disordered. (c) Image without trajectories of the $p/q = 1/1$ locking step for the same system at $\phi = 0.46$ and $\theta = 45^\circ$. (d) The system in Fig. 10(c) with $\phi = 0.57$ at $p/q = 1/1$, where there is no directional locking and the disk configuration is disordered.

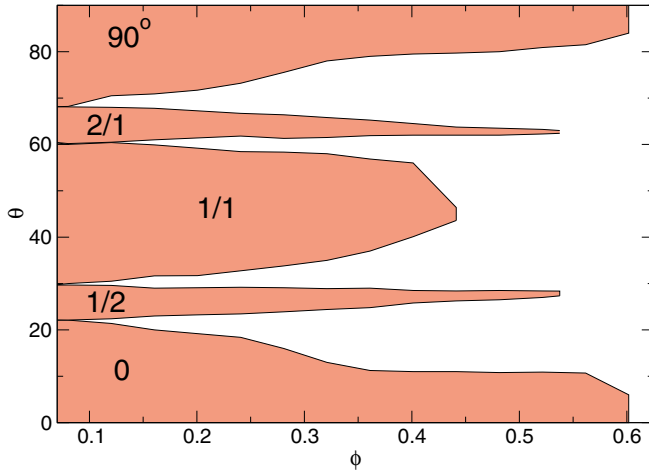


FIG. 12. Locked regions (shaded areas) as a function of θ vs ϕ for the system in Fig. 10 with $a = 4.0$, $F^D = 0.5$, $R_{\text{obs}} = 1.0$, and $R_d = 0.5$, showing directional locking at $p/q = 0, 1/2, 1/1, 2/1$, and 90° . The $1/1$ step is lost when $\phi > 0.4$.

for the nonlocking regime just above the $p/q = 1/2$ locking step. In Fig. 11(c) we plot the disk positions without trajectories for a sample with $\phi = 0.46$ at $\theta = 45^\circ$ on the $p/q = 1/1$ locking step, where the disks move in 1D channels oriented 45° from the x axis. The same system is shown at $\phi = 0.57$ in Fig. 11(d), where the locking step is absent and the disk configuration is disordered. As ϕ increases, ordered locking flow can occur at $p/q = 1/1$ as long as the chains of moving disks remain narrow enough to avoid colliding with the obstacles while moving. When the obstacle radius is small, the number n of rows of moving disks that can fit between the obstacles is limited by the diameter of the disks. Specifically, if n rows of disks are driven at an angle θ , obstacle-disk collisions can be avoided only if $nR_d + R_{\text{obs}} \leq \frac{a}{2} \cos \theta$, giving the criterion $n \leq (1/R_d)(\frac{a}{2} \cos \theta - R_{\text{obs}})$. For the system in Fig. 11 with $a = 4.0$, $R_d = 0.5$, and $R_{\text{obs}} = 1.0$, we obtain $n \leq 2$ when $\theta = 0$, indicating that locking of two rows can occur on the $p/q = 0$ step, while $n \leq 0.8$ when $\theta = 45^\circ$, showing that no locking occurs at $p/q = 1/1$.

In Fig. 12 we show the locations of the locking steps as a function of θ versus ϕ for the system in Fig. 10. There are only five steps, at $p/q = 0, 1/2, 1/1, 2/1$, and 90° . The $1/1$ step disappears when $\phi > 0.45$, the $1/2$ and $2/1$ steps vanish above $\phi = 0.55$, and the 0° and 90° steps persist up to $\phi = 0.6$. As R_{obs} increases, the number of locking phases decreases.

IV. VARIED OBSTACLE RADIUS AND CLOGGING

We next vary the radius of the obstacles while holding the lattice constant at $a = 4.0$ and fixing the number of mobile disks. As the obstacle radius decreases, we find a larger number of possible locking phases. In the inset in Fig. 13 we plot $\langle V_x \rangle$ and $\langle V_y \rangle$ versus θ for a system with $R_d = 0.5$, $R_{\text{obs}} = 0.025$, and $\phi = 0.1934$. Here $N_{\text{obs}} = 81$ and $N_d = 319$. A series of dips appears in the velocity curves at the edges of each locking phase, and on the $p/q = 1/1$ locking step we find $\langle V_x \rangle = \langle V_y \rangle$. In Fig. 13(b), we show the corresponding

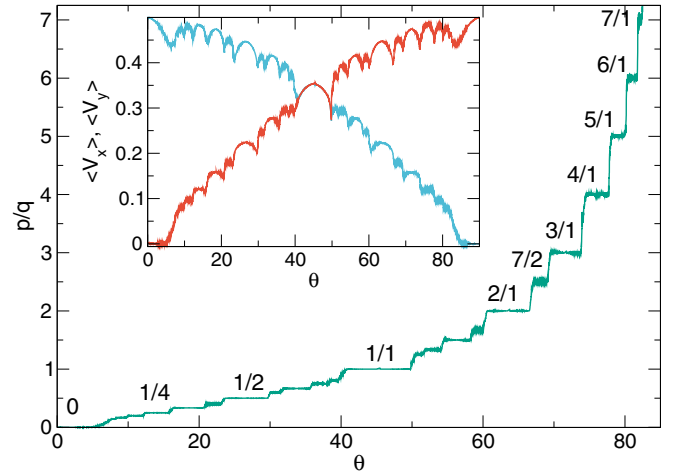


FIG. 13. p/q vs θ for the same system over the range $0 \leq \theta \leq 86^\circ$. Locking steps with $p/q = 0, 1/4, 1/1, 2/1, 7/2, 3/1, 4/1, 5/1, 6/1$, and $7/1$ are labeled. There is also another step at $p/q = 8/1$ which is not shown. Inset: $\langle V_x \rangle$ (blue curve) and $\langle V_y \rangle$ (red curve) vs θ for a system with $R_d = 0.5$, $R_{\text{obs}} = 0.025$, $a = 4.0$, and $\phi = 0.1934$.

p/q versus θ curve up to $\theta = 86^\circ$, with labels indicating the steps where $p/q = 0, 1/4, 1/1, 2/1, 7/2, 3/1, 4/1, 5/1, 6/1$, and $7/1$. There is an additional step at $p/q = 8/1$, which is not shown.

In Fig. 14 we show a blowup of the p/q versus θ curve in Fig. 13(b) to better illustrate the additional locking phases at $p/q = 0, 1/7, 1/6, 1/5, 1/4, 1/3, 2/5, 1/2, 3/5, 2/3, 3/4, 4/5, 1/1, 5/4, 4/3, 3/2, 5/3$, and $2/1$. As the obstacle density decreases, the number of possible p/q locking steps increases, as described in Sec. V. The presence of the higher-order values of p/q is limited by the radius and density of the mobile disks as well as by the system size. For example, if we increase the number of mobile disks so that ϕ is larger, the higher-order locking steps disappear.

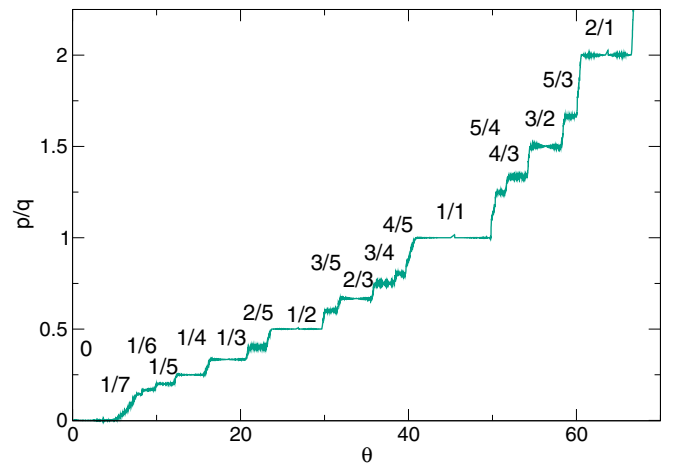


FIG. 14. A zoomed-in view of $p/q = \langle V_y \rangle / \langle V_x \rangle$ vs θ for the system in Fig. 13 with $R_d = 0.5$, $R_{\text{obs}} = 0.025$, $a = 4.0$, and $\phi = 0.1934$. Labels indicate the locking steps at $p/q = 0, 1/7, 1/6, 1/5, 1/4, 1/3, 2/5, 1/2, 3/5, 2/3, 3/4, 4/5, 1/1, 5/4, 4/3, 3/2, 5/3$, and $2/1$.

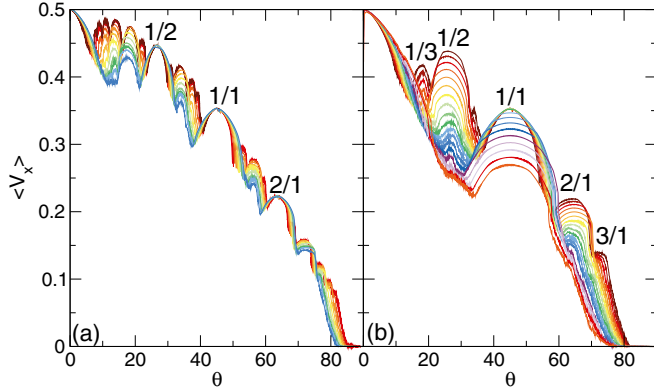


FIG. 15. (a) $\langle V_x \rangle$ vs θ curve for the system in Fig. 13 with $R_d = 0.5$, $a = 4.0$, and $\phi = 0.1934$ at $R_{\text{obs}} = 0.0125, 0.025, 0.05, 0.1, 0.15, 0.2, 0.25, 0.3, 0.35, 0.4$, and 0.45 , from top to bottom. (b) The same for R_{obs} ranging from $R_{\text{obs}} = 0.05$ to $R_{\text{obs}} = 1.45$ at intervals of 0.05 , from top to bottom. As R_{obs} increases, both the velocity and the number of steps decrease.

In Fig. 15(a) we plot $\langle V_x \rangle$ versus θ for the system in Fig. 13 for varied R_{obs} from $R_{\text{obs}} = 0.0125$ to $R_{\text{obs}} = 0.45$. At the $p/q = 1/2, 1/1$, and $2/1$ locking steps, $\langle V_x \rangle$ reaches the same maximum value regardless of the value of R_{obs} . At the maximum of each of these steps, the disks no longer collide with the obstacles so the velocity is insensitive to the obstacle radius. For other locking steps, there are always disk-obstacle collisions and therefore $\langle V_x \rangle$ decreases with increasing R_{obs} . In general, for each p/q step there is a particular value of R_{obs} above which $\langle V_x \rangle$ begins to decrease with increasing R_{obs} . The higher-order p/q locking phases also gradually disappear as R_{obs} increases.

In Fig. 15(b) we plot $\langle V_x \rangle$ versus θ for the same system as in Fig. 15(a) over the range $0.5 \leq R_{\text{obs}} \leq 1.45$. At the peak of the $p/q = 1/1$ locking step, the value of $\langle V_x \rangle$ remains constant for $R_{\text{obs}} \leq 0.9$, while for larger values of R_{obs} , $\langle V_x \rangle$ begins to decrease. The width of the $p/q = 1/1$ step increases with increasing R_{obs} up to $R_{\text{obs}} = 1.35$, after which it decreases again, while the steps with $p/q = 1/3, 1/2, 2/1$, and $3/1$ decrease in width until for $R_{\text{obs}} = 1.45$ they are absorbed by the $0^\circ, 90^\circ$, and $p/q = 1/1$ locking regimes.

In Fig. 16 we plot $\langle V_x \rangle$ versus θ for the same system in Fig. 15 at $R_{\text{obs}} = 1.45, 1.475, 1.5, 1.5125, 1.525, 1.55, 1.575, 1.5875, 1.6, 1.6025, 1.6075$, and 1.6375 . The velocity decreases with increasing R_{obs} and reaches 0 for $R_{\text{obs}} = 1.6375$. The $p/q = 1/1$ locking step is lost when $R_{\text{obs}} \geq 1.575$. For $R_{\text{obs}} = 1.6025$, the system reaches a clogged state near $\theta \approx 38^\circ$. In this regime, an increasing fraction of the sample contains mobile disk configurations that block the flow. When $R_{\text{obs}} \geq 1.6125$, the flow is blocked for all driving angles.

Figure 17 illustrates the disk configurations on the 0° locking step for different obstacle sizes, showing the evolution into a clogged state. At $R_{\text{obs}} = 0.75$ in Fig. 17(a), the disks form flowing 1D chains. In Fig. 17(b) at $R_{\text{obs}} = 1.4$, the disks interact more strongly with the obstacles but no clogging occurs. When $R_{\text{obs}} = 1.55$ as in Fig. 17(c), trimer configurations form between adjacent obstacles, intermittently blocking the flow. At $R_{\text{obs}} = 1.6125$ in Fig. 17(d), the system is in a

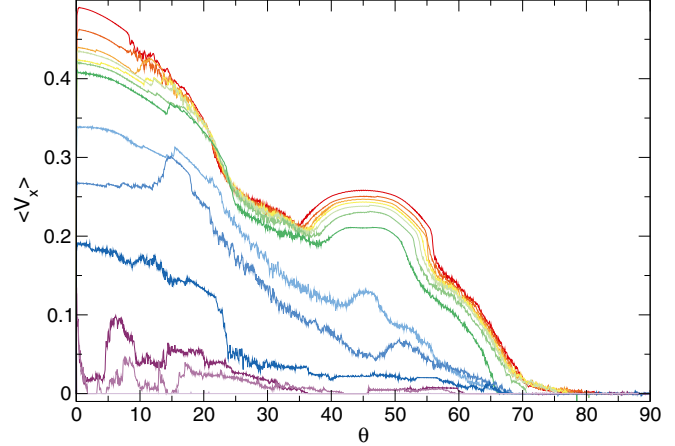


FIG. 16. (a) $\langle V_x \rangle$ vs θ for the system in Fig. 13 with $R_d = 0.5$, $a = 4.0$, and $\phi = 0.1934$ at $R_{\text{obs}} = 1.45, 1.475, 1.5, 1.5125, 1.525, 1.55, 1.575, 1.5875, 1.6, 1.6025, 1.6075$, and 1.6375 , from top to bottom. As R_{obs} increases, the system becomes clogged over a greater range of driving angles. At $R_{\text{obs}} = 1.5875$ and 1.6 , directional locking still occurs, while for $R_{\text{obs}} = 1.6375$, there is complete clogging at every driving angle.

completely clogged state. The local disk density is strongly heterogeneous in a clogged sample, with some regions of high disk density accompanied by other regions that contain no disks. The clogged state we observe is similar to that found for binary disks moving through periodic obstacle arrays [46]. For $R_{\text{obs}} = 1.6025$ and 1.6075 , the clogging is directionally

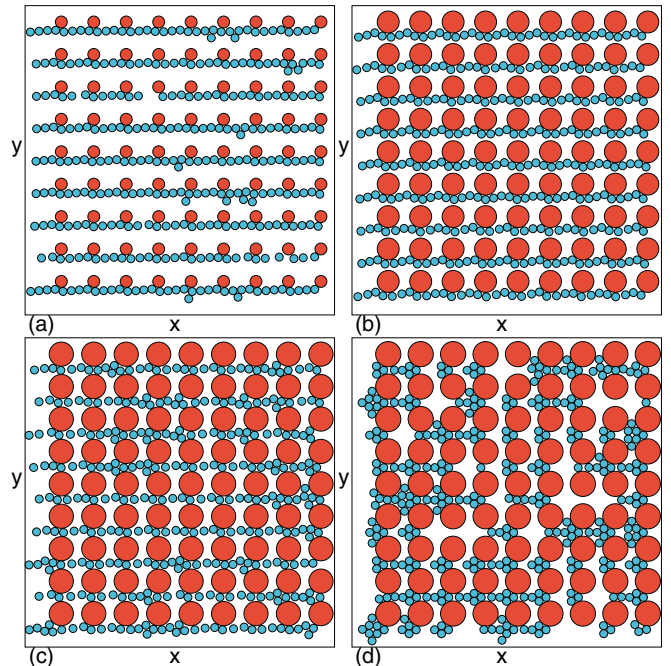


FIG. 17. Obstacle (red circles) and disk (blue circles) locations for the system in Figs. 15 and 16 with $R_d = 0.5$, $a = 4.0$, and $\phi = 0.1934$ in the 0° locking phase. (a) $R_{\text{obs}} = 0.75$. (b) $R_{\text{obs}} = 1.4$. (c) $R_{\text{obs}} = 1.55$, where partial clogging begins to occur. (d) $R_{\text{obs}} = 1.6125$, where there is a clogged state.

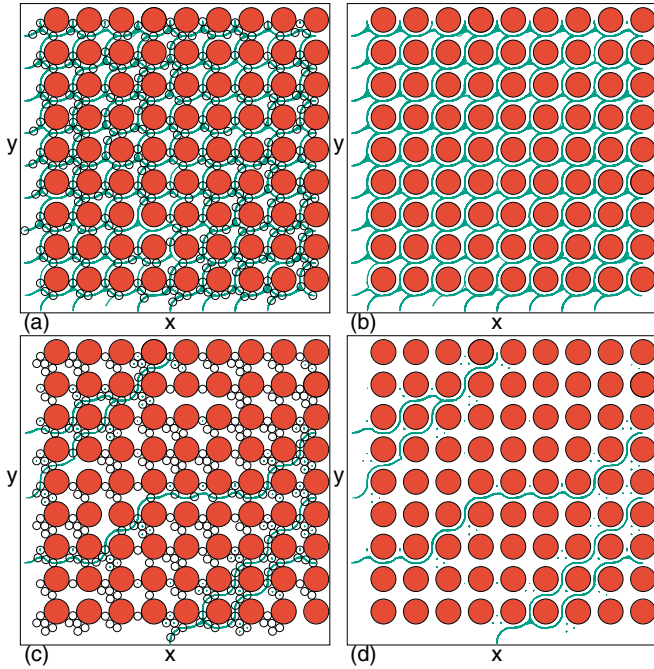


FIG. 18. (a) Obstacle (red circles) and disk (open circles) locations along with the disk trajectories (green symbols) for the system in Fig. 16 with $R_d = 0.5$, $a = 4.0$, and $\phi = 0.1934$ for $\theta = 40^\circ$. (a) $R_{\text{obs}} = 3.15$. (b) The same as (a), showing only the obstacles and the trajectories. (c) $R_{\text{obs}} = 3.2$. (d) The same as (c), showing only the obstacles and the trajectories, indicating that a partially clogged phase is present.

dependent and the system does not clog for flow along the x , y , or 45° directions but becomes completely blocked for flow at the other angles.

In Fig. 18(a) we plot the obstacle and disk configurations along with the trajectories at $\theta = 40^\circ$ in the system from Fig. 16 with $R_{\text{obs}} = 1.575$, while in Fig. 18(b) we show only the trajectories and obstacles. The disks are beginning to accumulate behind the obstacles but continue to flow around the obstacles, as indicated in Fig. 18(b). The obstacles, disk configurations, and trajectories for the same system with $R_{\text{obs}} = 1.6$ appear in Fig. 18(c), while Fig. 18(d) shows only the obstacles and trajectories. The system is in a partially clogged phase containing large regions where there is no flow interspersed with some winding channels. Those disks that continue to move channel predominantly along the 0° direction with occasional vertical jumping from one channel to the next.

The transition to a clogged state can be quantified by measuring $\langle V_x \rangle$ as a function of R_{obs} for a specific value of θ . In Fig. 19 we plot $\langle V_x \rangle$ versus R_{obs} for $\theta = 3^\circ$ and $\theta = 45^\circ$. When $\theta = 3.0^\circ$, the flow is locked along 0° and the velocity remains constant up to $R_{\text{obs}} = 1.45$, above which the velocity drops until reaching 0 near $R_{\text{obs}} = 1.61$. For $\theta = 45^\circ$, there is a smaller overall value of $\langle V_x \rangle$, which remains constant up to $R_{\text{obs}} = 0.9$, decreases linearly for $0.9 < R_{\text{obs}} < 1.54$, and then decreases more rapidly before reaching 0 near $R_{\text{obs}} = 1.61$. For other locking steps, we find a similar behavior in which $\langle V_x \rangle$ remains constant below a certain value of R_{obs} before decreasing linearly and then dropping rapidly to $\langle V_x \rangle = 0$ at

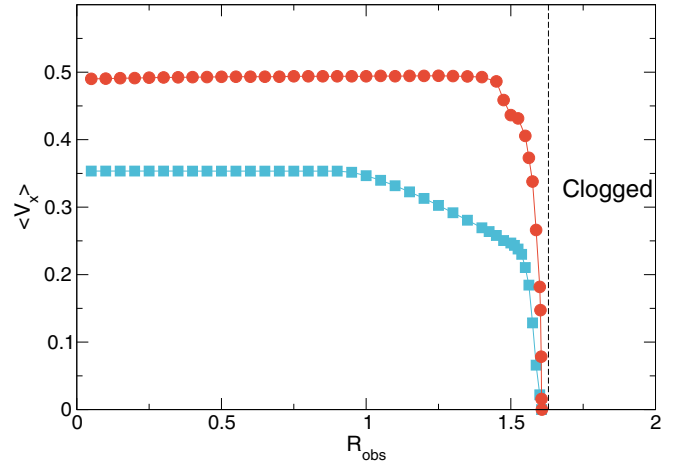


FIG. 19. $\langle V_x \rangle$ vs R_{obs} for a system with $R_d = 0.5$ and $a = 4.0$ on the 0° locking step at $\theta = 3^\circ$ (red circles) and on the $p/q = 1/1$ locking step at $\theta = 45^\circ$ (blue squares), showing the crossover from a constant value to a clogged state.

higher R_{obs} . In Fig. 20 we plot the step regions and clogged regions as a function of θ versus R_{obs} for the system in Fig. 16. We highlight the $p/q = 0, 1/3, 1/2, 1/1, 2/1, 3/1$, and 90° steps, where the step width in θ generally increases with R_{obs} up to some critical value of R_{obs} before decreasing again. The higher-order locking steps disappear for $R_{\text{obs}} > 0.5$. The 0° and 90° locking steps diminish in width near $R_{\text{obs}} = 1.45$, which is correlated with the onset of the partially clogged states.

We refer to the states in which the flow drops to 0 as clogged rather than jammed. Jamming typically describes amorphous systems composed of loose particles such as grains, emulsions, or disks which have no quenched disorder [47–52]. In 2D systems, jamming is typically associated with some type of long-range growing rigid correlation length due to the buildup of contact forces between the particles [51].

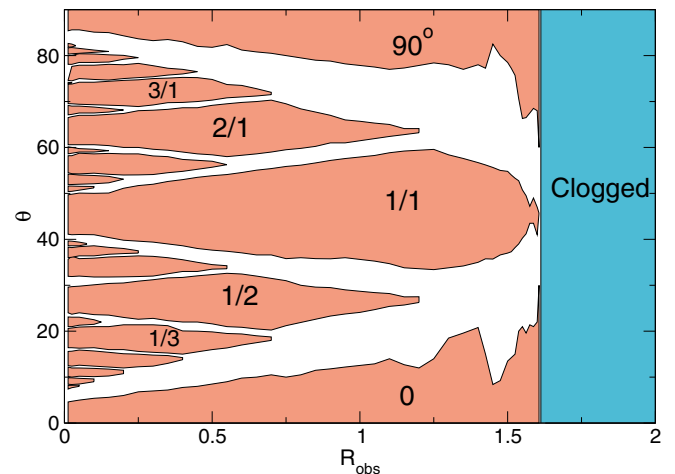


FIG. 20. Locked regions (pink area) and clogged region (blue area) as a function of θ vs R_{obs} for the system in Figs. 15 and 16 with $R_d = 0.5$ and $a = 4.0$. Locking steps with $p/q = 0, 1/3, 1/2, 1/1, 2/1$, and $3/1$ are labeled along with the 90° locking step.

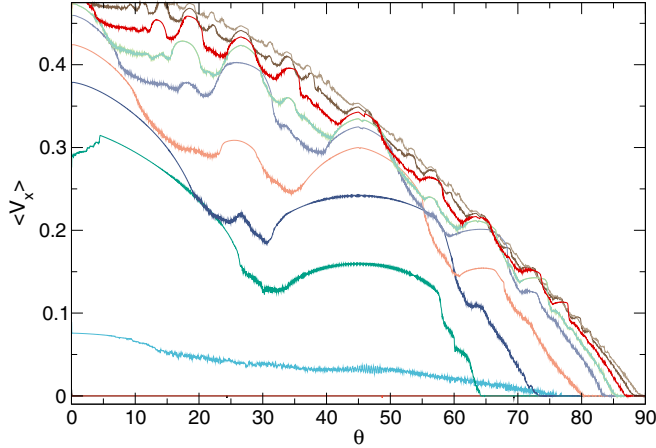


FIG. 21. $\langle V_x \rangle$ vs θ for samples with $N_d = 400$, $R_d = 0.5$, and $R_{\text{obs}} = 1.0$ at $a = 18, 12, 9, 7.2, 6.0, 4.5, 3.6, 3.0, 2.5$, and 2.25 , from top to bottom. At $a = 2.25$, the system is in a clogged state.

In a clogged system, the cessation of flow is more local and is associated with individual bottlenecks [53,54]. Clogging can occur for particles flowing through an individual hopper when the particles adopt an arched configuration near the mouth of the aperture. The susceptibility to clogging in this case increases as the width of the aperture decreases. In the clogging we observe, the flow stops when the distance between the obstacles is reduced due to an increase in R_{obs} , so the system can be regarded as a series of coupled hoppers.

The clogging we find is similar to the clogging phenomenon studied in disordered systems with random obstacle arrays. In the latter system, a critical density of obstacles is required to block the flow and the clogged states are inhomogeneous since the individual blocked particles produce higher-density pileups behind them while other regions of the sample contain few particles [46,55–57]. The clogged state forms for lower densities when the quenched disorder is random compared to systems containing periodic obstacle arrays [55–57]. When the driving is applied along the x direction with $\theta = 0$, the obstacles in a periodic obstacle lattice with an easy flow channel aligned in the x direction must have a fairly large radius in order to induce clogging, while at larger driving angles, the clogging is more similar to that found in systems with random obstacles. At finite temperature, the clogging is likely to be intermittent, with some clogged states breaking up thermally and flowing for a period of time before reforming. The clogging can also be disrupted by the application of an additional ac drive on top of the dc drive or by reversing the direction of the drive for a period of time. The clogging susceptibility also depends on the magnitude of the driving force F^D since the disks are harmonic, so that for weaker drives, the system can reach a clogged state at lower R_{obs} and lower ϕ . This property will be studied in another work.

V. VARIED OBSTACLE LATTICE CONSTANT

We next consider samples with fixed R_{obs} but varied a , focusing on a system with $N_d = 400$, $R_d = 0.5$, and $R_{\text{obs}} = 1.0$. In Fig. 21 we plot $\langle V_x \rangle$ versus θ for $a = 18, 12, 9, 7.2, 6.0, 4.5, 3.6, 3.0, 2.5$, and 2.25 . The velocity is highest for the largest a

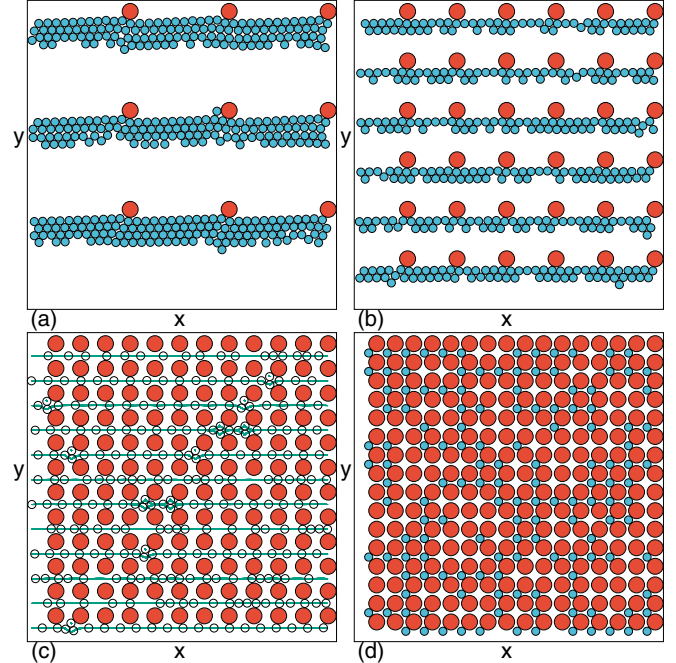


FIG. 22. Obstacle (red circles) and disk (blue and open circles) locations along with the disk trajectories (green symbols) for the system in Fig. 21 with $N_d = 400$, $R_d = 0.5$, and $R_{\text{obs}} = 1.0$ on the 0° locking step at a finite drive angle of $\theta = 2^\circ$. (a) $a = 12$. (b) $a = 6.0$. (c) $a = 3.0$, showing a partially clogged state. (d) $a = 2.25$, where there is a fully clogged state.

and the locking states appear as bumps. As a decreases, some of the locking steps such as those at $p/q = 1/1$ and $p/q = 1/2$ grow in width while the higher-order locking steps diminish in size. The extent of the $p/q = 1/2$ locking step begins to decrease when $a < 3.6$, and for $a = 3.0$, only the 0° , $p/q = 1/1$, and 90° locking phases appear. The system enters a partially clogged state at $a = 2.5$ and becomes fully clogged at $a = 2.25$. The evolution of the phases for decreasing a is similar to that found for fixed a and increasing R_{obs} , since in both cases the distance between the surfaces of the obstacles decreases.

In Fig. 22(a) we illustrate the disk configurations on the 0° locking step for a drive angle of $\theta = 2^\circ$ when $a = 12$, where the system forms a density-modulated stripe containing between three and four rows of disks. The stripes are pushed up against the obstacles due to the finite angle of the drive. Figure 22(b) shows the same system at $a = 6.0$, where the stripes are composed of between one and two rows of disks. In Fig. 22(c) at $a = 3.0$, the system forms a partially clogged state with a single row of disks flowing between the obstacles coexisting with several regions in which a trimer disk arrangement partially blocks the flow. The fully clogged state at $a = 2.25$, shown in Fig. 22(d), occurs when the obstacles are so dense that individual disks cannot pass between them. For higher F^D , the disks can effectively depin and move between the obstacles; this will be studied in another work.

At lower obstacle densities, we find various types of pattern formation at the locking phases, including states with a density gradient. In Fig. 23(a) we show the disk and obstacle locations for the system in Fig. 21 with $a = 9.0$ at $\theta = 10.5^\circ$

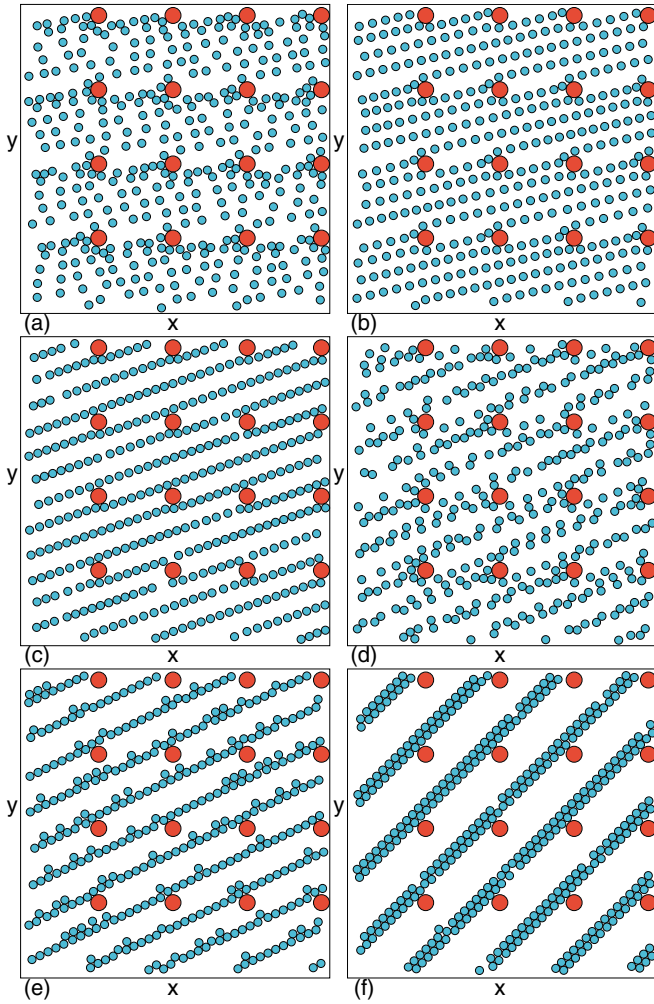


FIG. 23. Obstacle (red circles) and disk (blue circles) locations for the system in Fig. 21 with $N_d = 400$, $R_d = 0.5$, and $R_{\text{obs}} = 1.0$ at $a = 9.0$. (a) $\theta = 10.5^\circ$, in a nonlocking regime where a periodic gradient in the disk density arises. (b) The $p/q = 1/4$ locking phase. (c) The $p/q = 1/3$ locking phase. (d) A nonlocking phase between $p/q = 1/3$ and $p/q = 1/2$. (e) The $p/q = 1/2$ locking step. (f) The $p/q = 1/1$ locking step where a density-modulated stripe structure appears.

in a nonlocking state. The disks form a partial square lattice in the regions between the obstacles, while a disordered pileup of disks forms immediately behind each obstacle. On the $p/q = 1/4$ locking step in Fig. 23(b) at $\theta = 18.7^\circ$, the disks are more orderly and move in a series of channels, with a distortion in the rows produced by the deflection that occurs when the disks collide with the obstacles. In Fig. 23(c), which shows the $p/q = 1/3$ locking step, the disks move in nearly straight lines and undergo very few collisions with the obstacles. Figure 23(d) shows the disordered configuration in a nonlocking regime between the $p/q = 1/3$ and the $p/q = 1/2$ locking steps. On the $p/q = 1/2$ step in Fig. 23(e), the particles form a density-modulated phase, while in Fig. 24(f) at the $p/q = 1/1$ locking step, there are two rows of disks moving at 45° between the obstacles. We observe several ordered and disordered phases on the other locking steps.

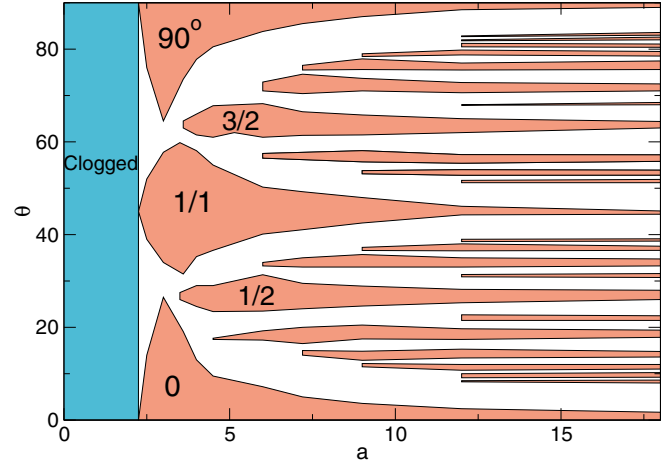


FIG. 24. Locked regions (pink area) and clogged region (blue area) as a function of θ vs a for the system in Fig. 21 with $N_d = 400$, $R_d = 0.5$, and $R_{\text{obs}} = 1.0$. Labels indicate the locations of the $p/q = 0, 1/2, 1/1, 3/2$, and 90° locking steps. Additional steps appear at $p/q = 1/7, 1/6, 1/5, 2/5, 1/4, 1/3, 3/5, 4/5, 6/5, 4/3, 5/2, 3/1, 4/1, 5/1, 6/1, 7/1$, and $8/1$.

In Fig. 24 we indicate the locations of the locking steps as a function of θ versus a for the system in Figs. 21 to 23, with labels denoting the clogged phase and the $p/q = 0, 1/2, 1/1, 3/2$, and 90° locking steps. Other locking steps also appear for $p/q = 1/7, 1/6, 1/5, 2/5, 1/4, 1/3, 3/5, 4/5, 6/5, 4/3, 5/2, 3/1, 4/1, 5/1, 6/1, 7/1$, and $8/1$. In systems that are larger in size than what we consider, additional locking phases with smaller widths appear at the larger values of a . For $2.25 < a \leq 3.0$, partial clogging phases occur, while for $a \leq 2.25$, there is a complete clogging phase. For $a > 3.0$, the widths of the 0° and 90° locking steps decrease approximately as $1/a$.

In Fig. 25 we plot the net velocity $\langle V \rangle$ versus θ for a system with $N_d = 400$, $R_{\text{obs}} = 0.5$, and $R_d = 0.5$ at $a = 12, 6, 4, 3$, and 2.25 . Here we have set $R_{\text{obs}} = 0.5$ in order to access higher disk densities. For $a = 12$, only small dips appear in $\langle V \rangle$, and for certain locking steps, $\langle V \rangle = F^D = 0.5$,

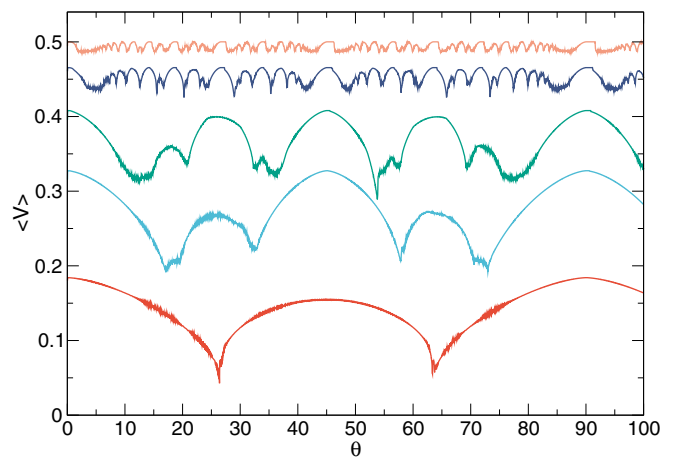


FIG. 25. Net velocity $\langle V \rangle$ vs θ for a system with $R_{\text{obs}} = 0.5$, $R_d = 0.5$, $N_d = 400$, and $a = 12, 6, 4, 3$, and 2.25 , from top to bottom.

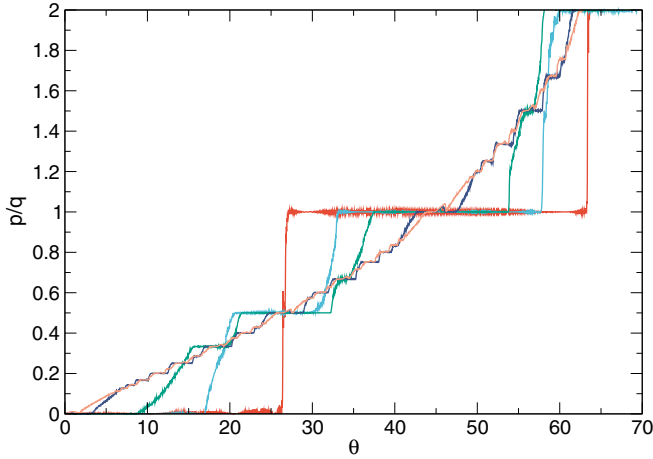


FIG. 26. p/q vs θ for the system in Fig. 25 with $R_{\text{obs}} = 0.5$, $R_d = 0.5$, and $N_d = 400$ plotted over the range $0 \leq \theta \leq 70^\circ$ and $0 \leq p/q \leq 2$ for $a = 12, 6, 4, 3$, and 2.25 , from upper left to lower left. There are fewer, wider steps for smaller a .

indicating that there are no collisions between the disks and the obstacles. As a decreases, the overall velocity drops. When $a = 4.0$, only the $p/q = 0, 1/3, 1/2, 1/1, 2/1, 3/1$, and 90° locking steps are present, while at $a = 3.0$, we find only the $p/q = 0, 1/2, 1/1, 2/1$, and 90° locking steps. For $a = 2.25$, only the three most robust steps of $p/q = 0^\circ, 1/1$, and 90° still appear. For smaller a , the system reaches a completely clogged state. In Fig. 26 we plot p/q versus θ for the system in Fig. 25, showing the growth of the locking phase step widths with decreasing a .

We have also examined samples with larger a values and higher disk densities and find density-modulated states similar to those described above. In Fig. 27 we show the disk configurations at $a = 6.0$, $R_d = 1.0$, $R_{\text{obs}} = 1.0$, and disk density $\phi = 0.525$. Figure 27(a) illustrates the 0° locking step where a disordered stripe phase appears. For a larger θ that is still within the 0° locking regime, the stripes become more compact and contain only four rows of disks. In Fig. 27(b) we plot the disk configuration on the $p/q = 1/5$ locking step, while in Fig. 27(c) we show the configuration at the $p/q = 1/3$ locking. Figure 27(d) gives an example of the configuration in the nonlocking regime just below the $p/q = 1/2$ locking step, while Fig. 27(e) shows the locking at $p/q = 1/1$ where the system forms an ordered state containing two rows moving at 45° . In Fig. 27(f) we illustrate the density-modulated state which forms at $p/q = 6/1$.

VI. RANDOM DILUTION

Finally, we test the robustness of the directional locking against a random dilution of the square obstacle array, achieved by randomly removing a fraction P_d of the obstacles. We consider a system with $R_d = 0.5$, $R_{\text{obs}} = 1.0$, $a = 4.0$, and $N_d = 30$ mobile disks, where the undiluted system has a density of $\phi = 0.2145$. In this case, strong locking appears at $p/q = 0, 1/2, 1/1, 2/1$, and 90° in the absence of dilution. In Fig. 28 we show the evolution of the steps in p/q versus θ as we randomly remove fractions $P_d = 0, 0.12, 0.247, 0.49$,

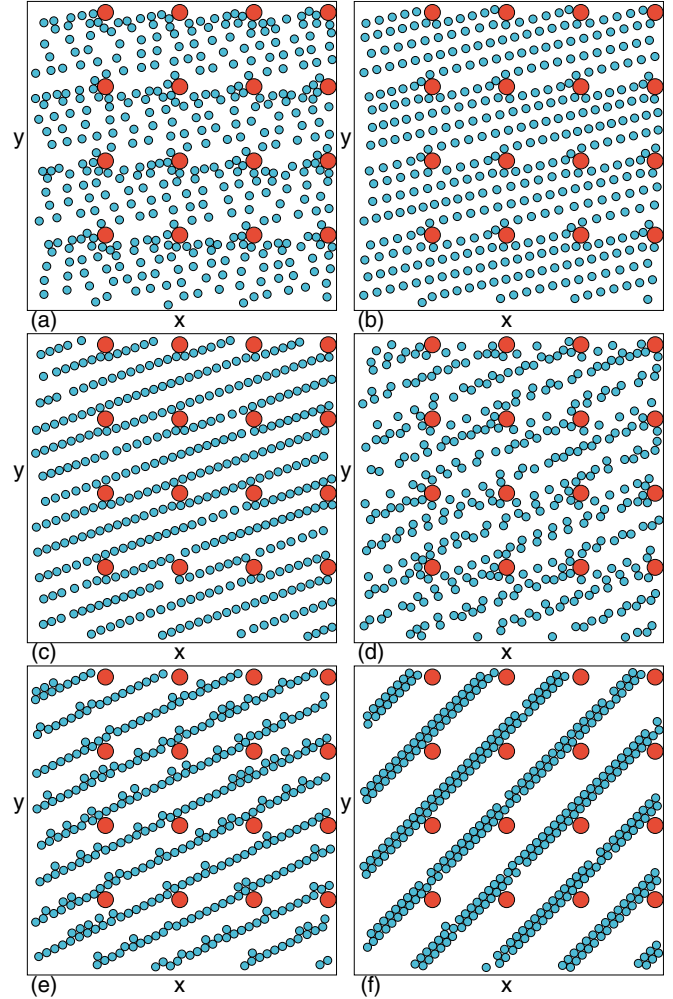


FIG. 27. Obstacle (red circles) and disk (blue circles) positions for a system with $a = 6.0$, $R_d = 0.5$, $R_{\text{obs}} = 1.0$, and density $\phi = 0.525$ showing pattern formation. (a) The 0° locking state. (b) $p/q = 1/5$ locking. (c) $p/q = 1/3$ locking. (d) A nonlocking phase just below the $p/q = 1/2$ step. (e) $p/q = 1/1$, where the system is ordered with two rows of disks. (f) $p/q = 6/1$, showing a density-modulated disk arrangement.

0.741, 0.925, and 1.0 of the obstacles. In general, the region of complete locking shrinks as the dilution fraction P_d increases; however, even for $P_d = 0.925$, the $p/q = 1/1$ locking regime remains visible, as highlighted in the inset in Fig. 28. For intermediate dilutions such as $P_d = 0.49$, additional steps at $p/q = 1/3$ and $4/3$ start to appear. These additional steps arise because the dilution produces an effect similar to that of decreasing the obstacle radius R_{obs} . There are also a number of smaller steps that arise with widths that depend on the exact configuration of the dilution. These results indicate that the directional locking is robust against dilution due to the presence of a strong long-range periodic component of the obstacle arrangement. Similar robustness of commensurability effects was observed previously in a superconducting vortex system [58,59] interacting with a randomly diluted periodic pinning array.

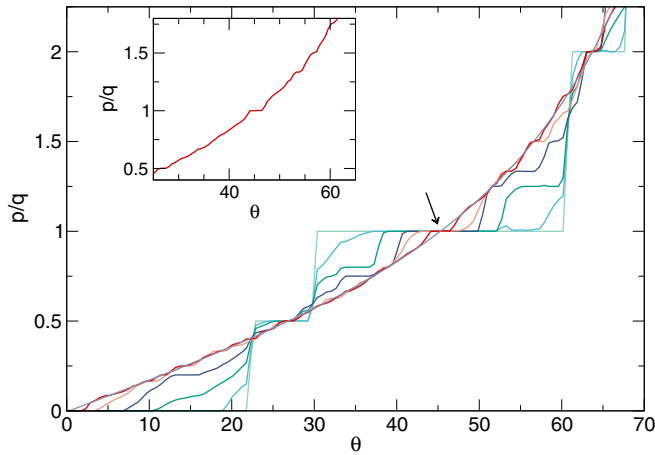


FIG. 28. The evolution of p/q vs θ for a system with $a = 4.0$, $R_d = 0.5$, $R_{\text{obs}} = 1.0$, and an undiluted density of $\phi = 0.2145$ as the fraction P_d of randomly removed disks is increased. $P_d = 0$ (light-green curve), 0.12 (light-blue curve), 0.247 (dark-green curve), 0.49 (dark-blue curve), 0.741 (orange curve), 0.925 (red curve), and 1.0 (light-purple curve). The arrow indicates the $p/q = 1$ locking step for motion along 45° . Inset: A zoom-in on the data in the main panel for only the $P_d = 0.925$ curve, showing that weak locking persists even when most of the obstacles have been removed.

VII. SUMMARY

We have examined the directional locking for a collection of disks moving through a square obstacle array, where we vary the mobile disk density, the obstacle radius, and the obstacle lattice constant. We find strong collective effects which produce a rich variety of patterns. On the steps with strong directional locking, such as 45° , the disks can form linear chains containing one or more rows. For other lock-

ing directions, we find square moving lattices or density-modulated states. The disk trajectories on the locking steps form ordered patterns and the disks move elastically without exchanging neighbors. In the nonlocking regimes, disordered or liquidlike states appear in which the disk trajectories mix. On the directional locking steps, the disk velocities are not fixed but form a parabolic shape with minima at the transitions into and out of the locked phase. In contrast, the ratio p/q describing the direction of motion is constant on each locking step. As the disk density increases, the number of possible locking phases diminishes due to the increasing frequency of disk-obstacle collisions, which makes it impossible for the disks to form a collectively moving pattern at certain drive angles. When the obstacle radius becomes larger, the number of locking steps decreases and the system first reaches a partially clogged phase in which a portion of the disks is stationary before entering a fully clogged state. For large obstacle lattice constants, a variety of moving stripe or density-modulated states appears on the locking steps, and the number of locking phases decreases with decreasing obstacle lattice constant until the system reaches a completely clogged state. Our results should be relevant to bubbles, emulsions, uncharged colloids, and magnetic textures moving through obstacle arrays, and they suggest a new way to dynamically generate stripe and density-modulated phases.

ACKNOWLEDGMENTS

This work was supported by the U.S. Department of Energy through the Los Alamos National Laboratory. Los Alamos National Laboratory is operated by Triad National Security, LLC, for the National Nuclear Security Administration of the U.S. Department of Energy (Contract No. 982333218NCA000001).

- [1] C. Reichhardt and F. Nori, Phase Locking, Devil's Staircases, Farey Trees, and Arnold Tongues in Driven Vortex Lattices with Periodic Pinning, *Phys. Rev. Lett.* **82**, 414 (1999).
- [2] J. Wiersig and K.-H. Ahn, Devil's Staircase in the Magnetoresistance of a Periodic Array of Scatterers, *Phys. Rev. Lett.* **87**, 026803 (2001).
- [3] P. T. Korda, M. B. Taylor, and D. G. Grier, Kinetically Locked-in Colloidal Transport in an Array of Optical Tweezers, *Phys. Rev. Lett.* **89**, 128301 (2002).
- [4] A. Gopinathan and D. G. Grier, Statistically Locked-In Transport Through Periodic Potential Landscapes, *Phys. Rev. Lett.* **92**, 130602 (2004).
- [5] M. P. MacDonald, G. C. Spalding, and K. Dholakia, Microfluidic sorting in an optical lattice, *Nature (London)* **426**, 421 (2003).
- [6] M. Balvin, E. Sohn, T. Iracki, G. Drazer, and J. Frechette, Directional Locking and the Role of Irreversible Interactions in Deterministic Hydrodynamics Separations in Microfluidic Devices, *Phys. Rev. Lett.* **103**, 078301 (2009).
- [7] S. Shapiro, Josephson Currents in Superconducting Tunneling: The Effect of Microwaves and Other Observations, *Phys. Rev. Lett.* **11**, 80 (1963).
- [8] S. N. Coppersmith and P. B. Littlewood, Interference Phenomena and Mode Locking in the Model of Deformable Sliding Charge-Density Waves, *Phys. Rev. Lett.* **57**, 1927 (1986).
- [9] A. Barone and G. Paterno, *Physics and Applications of the Josephson Effect* (Wiley, New York, 1982), p. 9.
- [10] C. Reichhardt and C. J. O. Reichhardt, Structural transitions and dynamical regimes for directional locking of vortices and colloids driven over periodic substrates, *J. Phys.: Condens. Matter* **24**, 225702 (2012).
- [11] L. R. Huang, E. C. Cox, R. H. Austin, and J. C. Sturm, Continuous particle separation through deterministic lateral displacement, *Science* **304**, 987 (2004).
- [12] C. Reichhardt and C. J. O. Reichhardt, Directional locking effects and dynamics for particles driven through a colloidal lattice, *Phys. Rev. E* **69**, 041405 (2004).
- [13] M. Pelton, K. Ladavac, and D. G. Grier, Transport and fractionation in periodic potential-energy landscapes, *Phys. Rev. E* **70**, 031108 (2004).
- [14] K. Ladavac, K. Kasza, and D. G. Grier, Sorting mesoscopic objects with periodic potential landscapes: Optical fractionation, *Phys. Rev. E* **70**, 010901(R) (2004).

- [15] A. M. Lacasta, J. M. Sancho, A. H. Romero, and K. Lindenberg, Sorting on Periodic Surfaces, *Phys. Rev. Lett.* **94**, 160601 (2005).
- [16] James P. Gleeson, J. M. Sancho, A. M. Lacasta, and K. Lindenberg, Analytical approach to sorting in periodic and random potentials, *Phys. Rev. E* **73**, 041102 (2006).
- [17] Y. Roichman, V. Wong, and D. G. Grier, Colloidal transport through optical tweezer arrays, *Phys. Rev. E* **75**, 011407 (2007).
- [18] B. R. Long, M. Heller, J. P. Beech, H. Linke, H. Bruus, and J. O. Tegenfeldt, Multidirectional sorting modes in deterministic lateral displacement devices, *Phys. Rev. E* **78**, 046304 (2008).
- [19] J. Koplik and G. Drazer, Nanoscale simulations of directional locking, *Phys. Fluids* **22**, 052005 (2010).
- [20] D. Speer, R. Eichhorn, and P. Reimann, Exploiting Lattice Potentials for Sorting Chiral Particles, *Phys. Rev. Lett.* **105**, 090602 (2010).
- [21] S. R. Risbud and G. Drazer, Directional locking in deterministic lateral-displacement microfluidic separation systems, *Phys. Rev. E* **90**, 012302 (2014).
- [22] B. H. Wunsch, J. T. Smith, S. M. Gifford, C. Wang, M. Brink, R. L. Bruce, R. H. Austin, G. Stolovitzky, and Y. Astier, Nanoscale lateral displacement arrays for the separation of exosomes and colloids down to 20 nm, *Nat. Nanotechnol.* **11**, 936 (2016).
- [23] T. S. H. Tran, B. D. Ho, J. n P. Beech, and J. O. Tegenfeldt, Open channel deterministic lateral displacement for particle and cell sorting, *Lab Chip* **17**, 3592 (2017).
- [24] K. Chen, O. J. Gebhardt, R. Devendra, G. Drazer, R. D. Kamien, D. H. Reich, and R. L. Leheny, Colloidal transport within nematic liquid crystals with arrays of obstacles, *Soft Matter* **14**, 83 (2018).
- [25] Y. Li, H. Zhang, Y. Li, X. Li, J. Wu, S. Qian, and F. Li, Dynamic control of particle separation in deterministic lateral displacement separator with viscoelastic fluids, *Sci. Rep.* **8**, 3618 (2018).
- [26] X. Li, C. Wu, T. Cao, and Y. Cao, Directional mode-locking of driven two-dimensional active magnetized colloids with periodic pinning centers, *Physica A* **515**, 279 (2019).
- [27] C. Reichhardt, D. Ray, and C. J. O. Reichhardt, Quantized transport for a skyrmion moving on a two-dimensional periodic substrate, *Phys. Rev. B* **91**, 104426 (2015).
- [28] J. Feilhauer, S. Saha, J. Tobik, M. Zelent, L. J. Heyderman, and M. Mruczkiewicz, Controlled motion of skyrmions in a magnetic antidot lattice, [arXiv:1910.07388](https://arxiv.org/abs/1910.07388).
- [29] N. P. Vizarim, C. Reichhardt, C. J. O. Reichhardt, and P. A. Venegas, Skyrmion dynamics and topological sorting on periodic obstacle arrays, *New J. Phys.* **22**, 053025 (2020).
- [30] A. Soba, P. Tierno, T. M. Fischer, and F. Saguès, Dynamics of a paramagnetic colloidal particle driven on a magnetic-bubble lattice, *Phys. Rev. E* **77**, 060401(R) (2008).
- [31] J. Loehr, M. Loenne, A. Ernst, D. de las Heras, and T. M. Fischer, Topological protection of multiparticle dissipative transport, *Nat. Commun.* **7**, 11745 (2016).
- [32] G. Volpe, I. Buttinoni, D. Vogt, H.-J. Kümmerer, and C. Bechinger, Microswimmers in patterned environments, *Soft Matter* **7**, 8810 (2011).
- [33] M. Brun-Cosme-Bruny, A. Förtsch, W. Zimmermann, E. Bertin, P. Peyla, and S. Rafai, Deflection of phototactic microswimmers through obstacle arrays, [arXiv:2005.05677](https://arxiv.org/abs/2005.05677).
- [34] C. Reichhardt and C. J. O. Reichhardt, Dynamical Ordering and Directional Locking for Particles Moving Over Quasicrystalline Substrates, *Phys. Rev. Lett.* **106**, 060603 (2011).
- [35] T. Bohlein and C. Bechinger, Experimental Observation of Directional Locking and Dynamical Ordering of Colloidal Monolayers Driven Across Quasiperiodic Substrates, *Phys. Rev. Lett.* **109**, 058301 (2012).
- [36] A. V. Silhanek, L. Van Look, S. Raedts, R. Jonckheere, and V. V. Moshchalkov, Guided vortex motion in superconductors with a square antidot array, *Phys. Rev. B* **68**, 214504 (2003).
- [37] J. E. Villegas, E. M. Gonzalez, M. I. Montero, I. K. Schuller, and J. L. Vicent, Directional vortex motion guided by artificially induced mesoscopic potentials, *Phys. Rev. B* **68**, 224504 (2003).
- [38] C. Reichhardt and C. J. O. Reichhardt, Transverse commensurability effect for vortices in periodic pinning arrays, *Phys. Rev. B* **78**, 180507(R) (2008).
- [39] G. Zechner, W. Lang, M. Dosmailov, M. A. Bodea, and J. D. Pedarnig, Transverse vortex commensurability effect and sign change of the hall voltage in superconducting $\text{YBa}_2\text{Cu}_3\text{O}_{7-\delta}$ thin films with a nanoscale periodic pinning landscape, *Phys. Rev. B* **98**, 104508 (2018).
- [40] P. Tierno, A Moire foray, *Nat. Phys.* **15**, 733 (2019).
- [41] X. Cao, E. Panizon, A. Vanossi, N. Manini, and C. Bechinger, Orientational and directional locking of colloidal clusters driven across periodic surfaces, *Nat. Phys.* **15**, 776 (2019).
- [42] F. Trillitzsch, R. Guerra, A. Janas, N. Manini, F. Krok, and E. Gnecco, Directional and angular locking in the driven motion of Au islands on MoS_2 , *Phys. Rev. B* **98**, 165417 (2018).
- [43] R. L. Stoop, A. V. Straube, T. H. Johansen, and P. Tierno, Collective Directional Locking of Colloidal Monolayers on a Periodic Substrate, *Phys. Rev. Lett.* **124**, 058002 (2020).
- [44] C. Reichhardt and C. J. O. Reichhardt, Dynamic regimes and spontaneous symmetry breaking for driven colloids on triangular substrates, *Europhys. Lett.* **68**, 303 (2004).
- [45] C. Reichhardt and C. J. O. Reichhardt, Switching and jamming transistor effect for vortex matter in honeycomb pinning arrays with ac drives, *Phys. Rev. B* **81**, 024510 (2010).
- [46] H. T. Nguyen, C. Reichhardt, and C. J. O. Reichhardt, Clogging and jamming transitions in periodic obstacle arrays, *Phys. Rev. E* **95**, 030902(R) (2017).
- [47] A. J. Liu and S. R. Nagel, Nonlinear dynamics—jamming is not just cool any more, *Nature (London)* **396**, 21 (1998).
- [48] M. E. Cates, J. P. Wittmer, J.-P. Bouchaud, and P. Claudin, Jamming, Force Chains, and Fragile Matter, *Phys. Rev. Lett.* **81**, 1841 (1998).
- [49] C. S. O'Hern, L. E. Silbert, A. J. Liu, and S. R. Nagel, Jamming at zero temperature and zero applied stress: The epitome of disorder, *Phys. Rev. E* **68**, 011306 (2003).
- [50] J. A. Drocco, M. B. Hastings, C. J. O. Reichhardt, and C. Reichhardt, Multiscaling at Point J : Jamming is a Critical Phenomenon, *Phys. Rev. Lett.* **95**, 088001 (2005).
- [51] C. Reichhardt and C. J. O. Reichhardt, Aspects of jamming in two-dimensional athermal frictionless systems, *Soft Matter* **10**, 2932 (2014).
- [52] A. L. Graves, S. Nashed, E. Padgett, C. P. Goodrich, A. J. Liu, and J. P. Sethna, Pinning Susceptibility: The Effect of Dilute,

- Quenched Disorder on Jamming, *Phys. Rev. Lett.* **116**, 235501 (2016).
- [53] I. Zuriguel, D. R. Parisi, R. C. Hidalgo, C. Lozano, A. Janda, P. A. Gago, J. P. Peralta, L. M. Ferrer, L. A. Pugnaloni, E. Clément, D. Maza, I. Pagonabarraga, and A. Garcimartín, Clogging transition of many-particle systems flowing through bottlenecks, *Sci. Rep.* **4**, 7324 (2015).
- [54] C. Barré and J. Talbot, Stochastic model of channel blocking with an inhomogeneous flux of entering particles, *Europhys. Lett.* **110**, 20005 (2015).
- [55] C. J. O. Reichhardt, E. Groopman, Z. Nussinov, and C. Reichhardt, Jamming in systems with quenched disorder, *Phys. Rev. E* **86**, 061301 (2012).
- [56] H. Peter, A. Libál, C. Reichhardt, and C. J. O. Reichhardt, Crossover from jamming to clogging behaviours in heterogeneous environments, *Sci. Rep.* **8**, 10252 (2018).
- [57] R. L. Stoop and P. Tierno, Clogging and jamming of colloidal monolayers driven across disordered landscapes, *Commun. Phys.* **1**, 68 (2018).
- [58] C. Reichhardt and C. J. O. Reichhardt, Commensurability effects at nonmatching fields for vortices in diluted periodic pinning arrays, *Phys. Rev. B* **76**, 094512 (2007).
- [59] M. Kemmler, D. Bothner, K. Ilin, M. Siegel, R. Kleiner, and D. Koelle, Suppression of dissipation in Nb thin films with triangular antidot arrays by random removal of pinning sites, *Phys. Rev. B* **79**, 184509 (2009).